Magnetic Study of Nanocrystalline TiB$_2$, TiC, B$_4$C Powders Doped to AISI 316L Austenitic Steel

T. Bodziony^{a,*}, S.M. Kaczmarek^a, A. Biedunkiewicz^b, G. Leniec^a and P. Figiel^b

^{a}Institute of Physics, West Pomeranian University of Technology, al. Piastów 17, 70-310 Szczecin, Poland

^{b}Institute of Materials Science and Engineering, West Pomeranian University of Technology,
al. Piastów 17, 70-310 Szczecin, Poland

The investigations into ferromagnetic resonance and magnetic susceptibility of nanocrystalline TiB$_2$, TiC, and B$_4$C powders (Ti–B–C system) doped to AISI 316L austenitic steel with different amounts (3 vol.%, 5 vol.% and 7 vol.%) have been carried out. The ferromagnetic resonance spectra were recorded in the temperature range from helium up to room temperature. The three tested composite samples contain a number of magnetic phases in different proportions. They reveal a structure originating from several different complex magnetic centers. The composites revealed such magnetic phenomena as paramagnetism, (anti)ferromagnetism, and superparamagnetism. Magnetic susceptibility investigations supported the ferromagnetic resonance studies and their analysis. Magnetic properties of the TiB$_2$, TiC, B$_4$C powders doped to AISI steel may play important role in further possible applications of these composite systems.

1. Introduction

Nanostructure materials often have unique chemical, structural, electrical, and magnetic properties [1–4] with potential applications including information storage [5], color imaging, bioprocessing, magnetic refrigeration [6, 7], and ferrofluids [8, 9]. Nanostructured materials exhibit a unique type of disorder. Very-low-energy regions (crystallites) exist at the expense of higher-energy boundary, interface, or surface regions. Magnetic nanoparticle and nanostructure studies cover a broad range of synthetic and investigative techniques from physics, chemistry, and materials science.

Our interest in magnetic study of nanostructure materials began with the study of TiC and TiN nanoparticles in different matrices [10–13]. Titanium carbide (TiC$_x$) and titanium nitride (TiN$_x$) are very important technological materials because being refractory materials they have gained much attention due to their extraordinary hardness. Titanium compounds are used in cutting tools and high-temperature alloys for a wide range of engineering applications. These compounds are the most intensively studied, both experimentally and theoretically, with regard to their physical properties. Titanium diboride (TiB$_2$) has attracted great interest due to its excellent mechanical properties, chemical resistance and good thermal and electrical conductivities. Fracture and wear resistance of TiC–TiB$_2$ composites obtained from TiB$_2$ and TiC powders is higher than that of single TiB$_2$ and TiC phases. For this reason, these composites are used for manufacturing matrices and cutting tools as well

as heat exchanger elements and combustion engine elements [14, 15].

The previous study of nanocrystalline powders suggests that mainly TiB$_2$, TiC and B$_4$C compounds are presented in the Ti–B–C systems doped to AISI 316L austenitic steel [4, 5]. Titanium diboride (TiB$_2$) and core-shell type TiC/C are characterized by many crystallographic and magnetic phases. These materials are widely studied because of their unusual properties including magnetic properties. The paper deals with the study of nanocrystalline TiB$_2$, TiC and B$_4$C powders doped to AISI 316L austenitic steel. The temperature dependence on the FMR spectra of samples is presented and discussed. Additionally, the magnetic susceptibility measurements have been carried out and their results have been compared with FMR measurements.

2. Experimental

Three samples numbered 7, 8, 9 with different content of magnetic impurities were synthesized. Nanocrystalline B$_4$C/TiB$_2$ and TiC/TiB$_2$ composite powders were synthesized by a non-hydrolytic sol–gel method. The synthesis was carried out in two stages. In the first, low-temperature stage, the precursor was obtained. In the second, high-temperature stage, the synthesis of ceramic phases under argon atmosphere was carried out. TiC$_x$N$_{1-x}$, TiB$_2$ and B$_4$C were obtained in this system, depending on initial precursor composition, temperature and time. After these processes the nanocrystalline powders were added to 316L austenitic steel. The details of preparation of the Ti–B–C system were described elsewhere [14]. The samples were characterized using X-ray diffraction (XRD) and scanning electron microscopy (SEM) methods. Moreover, these samples were studied by using temperature variable ferromagnetic resonance

———————

*corresponding author; e-mail: Tomasz.Bodziony@zut.edu.pl

(FMR) method and the magnetic susceptibility measurements.

Magnetic resonance absorption measurements were carried out with a conventional X-band ($\nu = 9.43$ GHz) Brucker E 500 spectrometer with 100 kHz magnetic field modulation. The measurements were performed in the temperature range from helium to room temperature with $\Delta T = 0.1$ K stability using an Oxford cryogenic system. Magnetic susceptibility measurements were carried out with a MPMS-7 SQUID magnetometer in the temperature range 4–300 K and magnetic fields up to 10 kOe in the zero-field-cooling (ZFC) and field cooling (FC) modes.

3. Results and discussion

We focused on the investigation of the samples marked as 7, 8, and 9. These are the composites of austenite steel 316L containing 3%, 5% and 7% Ti–B–C system, respectively. Ti–B–C system consists of titanium boride (TiB_2), titanium carbide (TiC) and B_4C ceramics powders. Austenitic steel type 316L is an extra-low carbon version of austenitic chromium nickel stainless steel containing molybdenum. 316L austenitic steel consists of: chromium 16–18%, nickel 10–14%, molybdenum 2–3% plus trace amounts of carbon, nitrogen, manganese, phosphorus, sulfur, silicon (information based on Product Data Sheet 316/316L Stainless Steel). XRD spectrum of composite Ti–B–C system (20 vol.%) and 316L austenite steel reveals the presence of titanium boride (TiB_2), austenite, ferrite, titanium carbide (TiC) and Cr_7C_3 peaks.

The representative examples of FMR spectra of samples 7 and 9 recorded at different temperatures are presented in Fig. 1 and Fig. 2, respectively. The intense and slightly asymmetric shape of FMR spectrum is clearly visible. It can be noticed that the FMR resonance line is much more intense at both low and high temperatures in sample 9 than in sample 7. Additionally, the FMR spectra of sample 9 have more asymmetric shape than the FMR spectra of sample 7 (see Figs. 1 and 2). Samples 7 and 9 have low or high admixture of ceramics powders, respectively. The FMR spectra of sample 8 are similar to those of sample 9 and therefore are not shown.

Figure 3 shows the examples of FMR spectra of the samples 7, 8, and 9 at two different temperatures: low temperature, about 10 K, and high temperature, about 240 K, for comparison. The asymmetries of the overlapped lines can be explained by assuming that the spectrum is a superposition of several separate resonance lines. It can be seen that asymmetries grow with increase of concentration of impurities. It should be noticed that sample 8 FMR spectrum behavior is different from that of other samples. FMR spectrum of sample 8 with 5% of impurities is much more intense than the spectrum of sample 9 with 7% of impurities in low temperature range (see Fig. 3).

It is easy to notice that main resonance line splits into two lines when the temperature increases to about
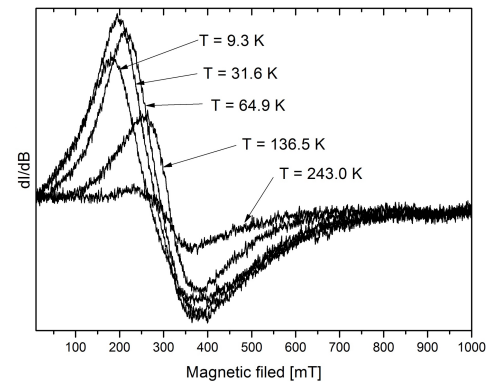

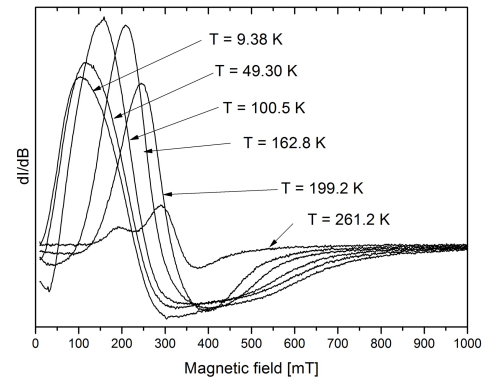Fig. 1. FMR spectra of sample 7 recorded at different temperatures.

Fig. 2. FMR spectra of sample 9 recorded at different temperatures.

260 K for sample 9 (see Figs. 2 and 3). The FMR spectra of samples 7 and 9 suggest that the resonance signal may originate from several different magnetic centers. However, we cannot rule out other possibilities such as high conductivity of the samples. Trivalent Ti^{3+} complexes in nanocrystalline TiC/C systems were detected previously [10, 11]. The addition of boron (B) to noncrystalline samples formed molybdenum–titanium–carbide (Mo–Ti–C) system, significantly changed the ap-
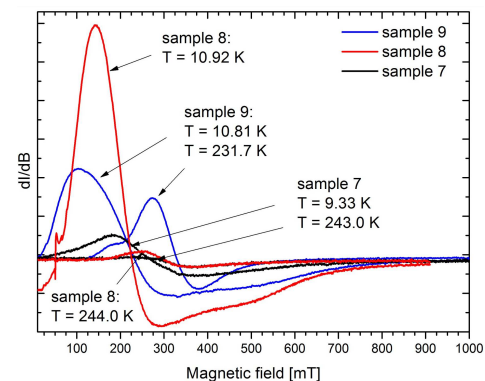

Fig. 3. The comparison of FMR spectra of sample 7, 8, and 9 at low ≈ 10 K and in high ≈ 240 K temperature ranges.

pearance and the temperature dependence of the FMR spectra of the Mo–Ti–C system, and increased the number of paramagnetic centers [10–13]. Boron is the element whose properties place it on the borderline between metals and non-metals (semimetallic).
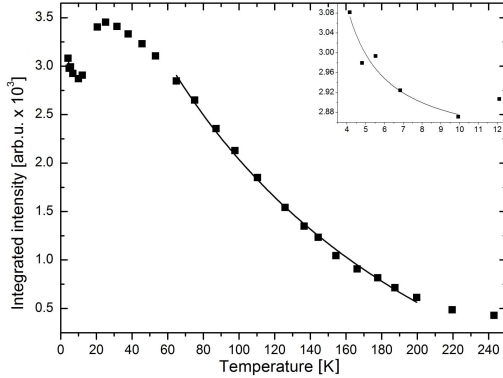

Fig. 4. The temperature dependence of the integrated intensity of the FMR spectra for sample 7. The two fitted Curie–Weiss curves (solid lines) in the temperature ranges: from 66 to 200 K and from 4 to 10 K are marked in main part and inset, respectively.
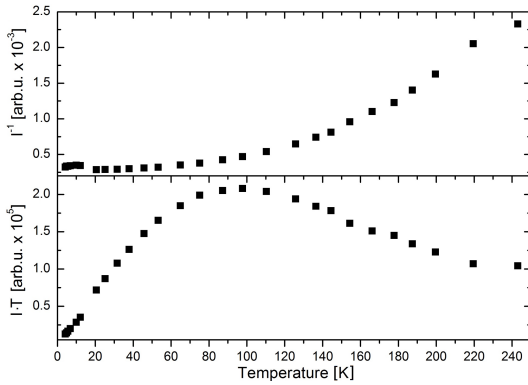

Fig. 5. The temperature dependence of the inverse integrated intensity of the FMR spectra (upper part) and the product of integrated intensity and temperature (lower part) for sample 7.

Figure 4 shows the temperature dependence on the integrated intensity of the FMR spectra of sample 7. The integrated intensity was obtained either by numerical integration of the FMR absorption spectra or by double numerical integration of the first derivative spectrum usually registered by the EPR spectrometer. There are a few types of behavior of integrated intensity. Firstly, the integrated intensity decreases with the increase of temperature from 4 K up to 9.93 K. Secondly, the integrated intensity increases reaching its maximum at 25.2 K. Above this point, the integrated intensity decreases with the increase of the temperature (see Fig. 4). However, this decrease is not homogeneous. The integrated intensity points are very well fitted by the Curie–Weiss curves in the low temperature range from 4 K to 10 K (Fig. 4, inset) and in the high temperature range between 63 K

and 200 K (Fig. 4). The Curie–Weiss law

$$I_{\mathrm{CW}}(T) = \frac{\mathrm{const}}{T - \Theta_{\mathrm{CW}}} \tag{1}$$

describes the behavior of the integrated intensity correctly only in these two ranges. The calculated Curie temperature $\Theta_{\mathrm{CW}} = 2.0 \pm 1.8$ K means that the ferromagnetic interaction dominates for the low temperature range. The calculated Curie temperature $\Theta_{\mathrm{CW}} = -135 \pm 28$ K is negative for the high temperature range between 63 K and 200 K. Figure 5 shows the temperature dependence on the inverse of integrated intensity ($I^{-1}(T)$, upper part) and the product of the integrated intensity with temperature ($I\,T(T)$, lower part). These kinds of dependences may reveal the presence of different magnetic interactions in the investigated systems.

One can see the upswing of the inverse of integrated intensity of the FMR spectra in the temperature range of 12–20 K and the nonlinear increase with increasing temperatures (Fig. 5, upper part). The product of the integrated intensity of the FMR spectra with temperature ($I\,T(T)$) is proportional to square of the effective magnetic moment. Three temperature ranges reveal different magnetic interactions as illustrated in Fig. 5 lower part. Magnetic moment increases with the temperature increasing up to ≈ 100 K. This may confirm that the antiferromagnetic interaction dominates below ≈ 100 K. Above the maximum of 97.75 K the magnetic moment decreases with the temperature growth, which indicates a prevailing ferromagnetic interaction. There are small differences visible for the temperature above 220 K. It can be said that there is another range above 220 K. This behavior was unidentified due to insufficient data.
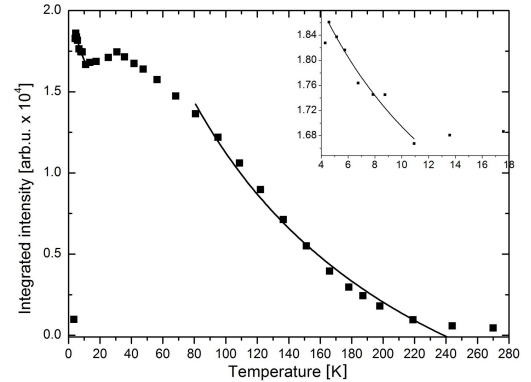

Fig. 6. The temperature dependence of the integrated intensity of the FMR spectra for sample 8. The two fitted Curie–Weiss curves (solid lines) in the temperature ranges: from 81 to 244 K and from 4.6 to 11 K are marked in main part and inset, respectively.

Figure 6 presents the temperature dependence on the integrated intensity of the FMR spectra $I(T)$ for sample 8. The temperature dependence on the integrated intensity of the FMR spectra $I(T)$ for sample 8 is very similar to the previously described sample 7. The first point at 3.44 K is different. The integrated intensity points are very well fitted by the Curie–Weiss curves in

TABLE I

The Curie temperature obtained from fitting of the Curie–Weiss law to the integrated intensity of the FMR spectra curve for samples 7, 8, 9.

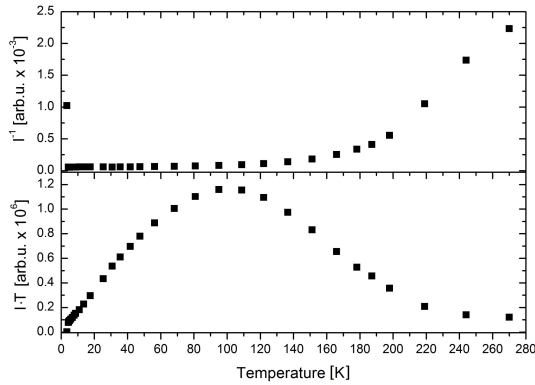| Sample	Θ_{CW} [K] at temperature range	
	low	high
7	4–10 $\quad\quad$ 2.0±1.8	63–200 $\quad\quad$ −135±28
8	4.6–11 $\quad\quad$ −10.7±15.5	81–244 $\quad\quad$ −89±42
9	—— $\quad\quad$ ——	120–270 $\quad\quad$ −288±105

Fig. 7. The temperature dependence of the inverse integrated intensity of the FMR spectrum (upper part) and the product of integrated intensity and temperature (lower part) for sample 8.

the temperature range from 4.6 K to 11 K and in the high temperature range between 81 K and 244 K (see Fig. 6, inset). The Curie temperatures are gathered in Table I. The temperature dependence on the inverse of integrated intensity of the FMR spectra ($I^{-1}(T)$, upper part) and the product of the integrated intensity of the FMR spectra with temperature ($I\,T(T)$, lower part) for sample 8 are shown in Fig. 7.
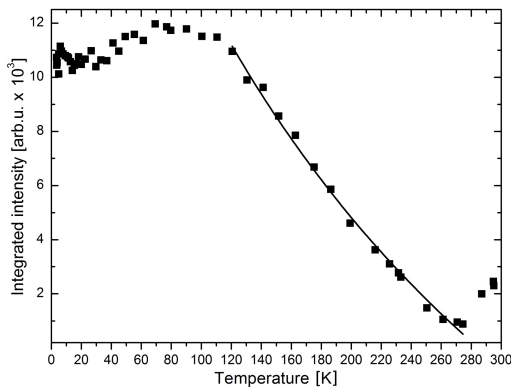

Fig. 8. The temperature dependence of the integrated intensity of the FMR spectra for sample 9. The fitted Curie–Weiss curve (solid line) in the temperature range from 120 to 275 K is marked.

Figure 8 shows the temperature dependence on the integrated intensity of the FMR spectra for sample 9. The temperature is varied from helium (≈ 4 K) up to room temperature. Three regions are visible in Fig. 8. The integrated intensity of the sample 9 increases with the increase of temperature in the low temperature range from ≈ 4 up to 70 K. However, the behavior of the integrated intensity of sample 9 is not clearly visible below ≈ 20 K. The integrated intensity of the FMR spectra decreases with the temperature increase up to 260 K after reaching its maximum at 70 K. In the third region above 260 K, the integrated intensity increases again as the temperature grows (see Fig. 8). The integrated intensity points are very well fitted by the Curie–Weiss law in the temperature range between 120 and 270 K. The Curie temperature is presented in Table I.

Figure 9 presents the temperature dependence on the inverse integrated intensity of the FMR spectrum ($1/I(T)$, lower part) and the temperature dependence on the product of integrated intensity and temperature ($I(T)\,T$, upper part) for sample 9.
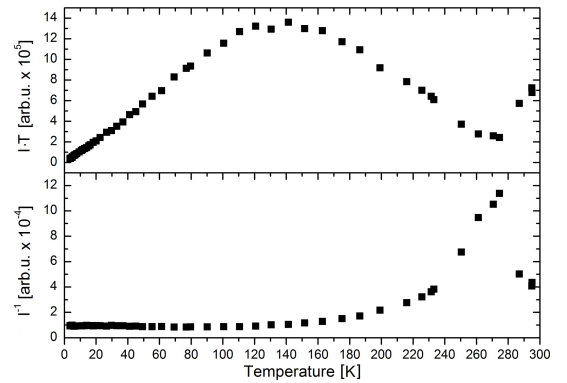

Fig. 9. The temperature dependence of the inverse integrated intensity of the FMR spectra (lower part) and the product of integrated intensity and temperature (upper part) for sample 9.
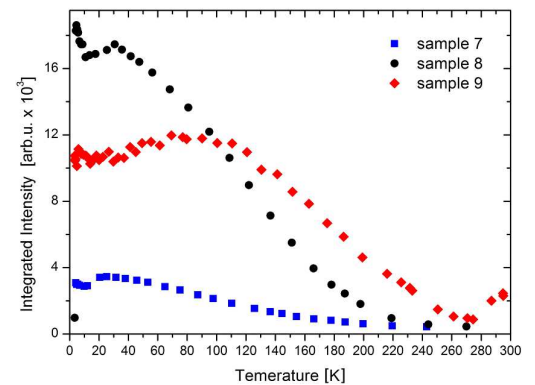

Fig. 10. The comparison of the integrated intensity of the FMR spectra for samples 7, 8, and 9.

The comparison of the integrated intensity of the FMR spectra for samples 7, 8, and 9 is shown in Fig. 10. It
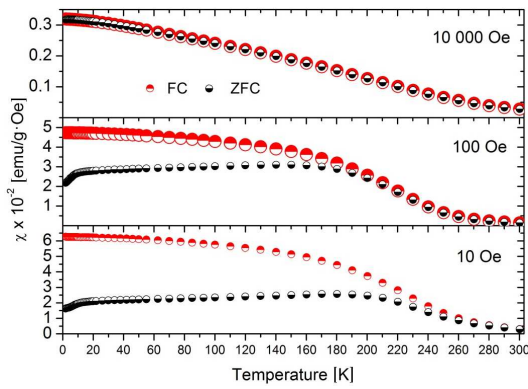
Fig. 11. Magnetic susceptibility measured in FC and ZFC modes in magnetic fields $H = 10$ Oe (lower part), $H = 100$ Oe (middle part) and $H = 10\,000$ Oe (upper part) for sample 9.

can be seen that the integrated intensity of the FMR spectra of sample 9 is much greater than the integrated intensity of sample 7 in the temperatures of up to about 200 K. The integrated intensities of samples 7 and 9 are nearly the same at temperature above 200 K. In spite of this, the integrated intensity of sample 8 is greater than that of sample 9 at temperature below ≈ 100 K. The integrated intensity of the FMR spectra of sample 8 is between integrated intensity of sample 9 and 7 only at temperature above 100 K (see Fig. 10).

Figure 11 shows the temperature dependences of dc magnetic susceptibility measured in FC and in ZFC modes in magnetic fields $H = 10$ Oe (lower part), $H = 100$ Oe (middle part) and $H = 10000$ Oe (upper part). Large differences between ZFC and FC magnetization branches below certain temperature of irreversibility indicate the presence of a strong magnetic anisotropy [16]. ZFC branches exhibit a broad maximum at temperature ≈ 180 K for very weak magnetic field 10 Oe (see Fig. 11, lower part). ZFC branches exhibit a broad and soft maximum at temperature $T \approx 140$ K for magnetic field $H = 100$ Oe, too (Fig. 11, middle part). The magnetization measured in ZFC mode at low temperatures (below ≈ 160 K) saturates and decreases further (for temperature below ≈ 20 K) for low magnetic fields: 10 and 100 Oe. It can be seen that the magnetization measured at FC mode approaches saturation only for very weak magnetic field 10 Oe and constantly increases for weak and strong magnetic fields 100 and 10000 Oe. The third magnetic susceptibility measured at strong magnetic field $H = 10000$ Oe shows no peaks (Fig. 11, upper part). Data points taken in FC and ZFC modes are difficult to distinguish.

Generally, the ZFC susceptibility shows a peak for both superparamagnets and spin glasses. It is usually seen that the temperature dependence on the FC susceptibility becomes saturated below the peak temperature (freezing temperature T_f) for spin glasses and continues to increase below that temperature (blocking temperature T_B) for superparamagnets [17]. Separation of ZFC

and FC curves in low temperature range indicates the presence of magnetic anisotropy that is removed only in high magnetic field — 10000 Oe (Fig. 11, upper part).

The evolutions of the integrated intensity of FMR spectra of samples: 7, 8, 9 are presented in Figs. 4, 6, 8, and together in Fig. 10. These dependences are similar. Temperature evolutions of integrated intensity of FMR spectra can be divided into three main groups. Integrated intensity of the FMR decreases with the temperature increase in the low temperature range, for example in the interval 4.6–11.0 K for sample 8. The Curie–Weiss law is fulfilled in this interval. Then, the integrated intensity starts to increase with the temperature growth until it reaches its maximum. There is a second interval, from 11.0 K to 31 K for sample 8 (Figs. 6, 9). This temperature may be called blocking temperature and is different for each sample. The maximum of the integrated intensity occurs at temperatures ≈ 25 K, ≈ 31 K, ≈ 90 K for sample 7, 8, and 9, respectively. It can be observed that the blocking temperature increases with the growing amount of impurities. In the third interval, above the blocking temperature, the integrated intensity decreases with the temperature increase. However, the rate of decline varies. The Curie–Weiss law is fulfilled in some temperature ranges in different samples. In addition, an increase of the integrated intensity FMR is observed in high temperatures, for example in sample 9. There is also a fourth range. It can be said that in each interval different magnetic interaction dominates. The Curie temperatures in low temperature range have positive and negative signs for samples 7 and 8, respectively (see Table I). This denotes the presence of ferromagnetic and antiferromagnetic interaction in sample 7 and 8 in the range of low temperatures. It seems that the paramagnetic ions, such as trivalent Ti^{3+}, may be responsible for these (anti)ferromagnetic interactions.

The growth of the integrated intensity with an increasing amount of dopant shows that impurities or possible composite impurities containing iron (Fe) or chromium (Cr) from steel are responsible for magnetic interactions. Abnormally high intensity of sample 8 shows that there exists a unique amount of impurity in steel in which magnetic interactions are extremely strong. The temperature dependences of the product of the integrated intensity ($I\,T(T)$) reveals similar behavior: an increase, a maximum and then a decrease (see Figs. 5, 9, 11). The increase and decrease are approximately linear. Maximum occurs at ≈ 100 K for samples 7, 8, and ≈ 140 K for sample 9. It means that the magnetic moment increases with the temperature increasing up to a maximum. This may confirm that the antiferromagnetic interaction dominates below a maximum. Above the maximum the magnetic moment decreases as the temperature grows, which indicates a prevailing ferromagnetic interaction. There are small differences visible for the temperature above 220 K in sample 9. It can be assumed that there is another range above 220 K. The temperature dependences of the product of the integrated intensity ($I\,T(T)$) con-

firm (anti)ferromagnetic interactions in wide intervals of temperatures in all three samples.

We suggest that superparamagnetic phase of nanoparticles is consistently responsible for behavior observed by means of the two methods used: FMR and SQUID in the temperature range between ≈ 20 K and ≈ 240 K with the characteristic blocking temperature. The magnetic susceptibility measurements also revealed the presence of the anisotropy field. Magnetic anisotropy is smoothed out by thermal fluctuation at high temperature. Paramagnetic, (anti)ferromagnetic and superparamagnetic phases and interaction are observed in tested samples 7, 8, 9 in all temperature ranges.

4. Conclusions

Three samples of nanocrystalline TiB_2, TiC, B_4C powders (3%, 5%, 7%) doped to AISI 316L austenitic steel were prepared. The three tested samples contained a number of crystalline and magnetic phases in different proportions. The FMR measurements were carried out in the 4–300 K range. Magnetic susceptibility measurements were made as well. The FMR measurements were taken in the temperature range from helium up to room temperature. The changes of the integrated intensity of FMR spectra versus temperature were analyzed. The temperature dependence on the integrated intensity of the FMR spectra of the investigated composites revealed different magnetic phenomena such as paramagnetism, (anti)ferromagentism, and superparamagnetism. Magnetic susceptibility measurements partially confirmed results of FMR studies. Magnetic properties of the TiB_2, TiC, B_4C powders doped to AISI steel are important because these kinds of composite may find broad applications in various technical devices in the future.

References

[1] R.W. Siegel, *Nanostruct. Mater.* **3**, 1 (1993).

[2] H. Gleiter, *Prog. Mater. Sci.* **33**, 223 (1989).

[3] V.G. Gryaznov, L.I. Trusov, *Prog. Mater. Sci.* **37**, 289 (1993).

[4] J. Dormann, D. Fiorani, *Magnetic Properties of Fine Particles*, North-Holland, Amsterdam 1992.

[5] R.D. Shull, *IEEE Trans. Magn.* **29**, 2614 (1993).

[6] R.D. Shull, R.D. McMichael, J.J. Ritter, L.J. Schwartzendruber, L.H. Bennett, in: *Proc. 7th Int. Cryocoolers Conf.*, Ed. M. Stoyanof, New Mexico 1993, p. 1133.

[7] R.F. Ziolo, E.P. Giannelis, B.A. Weinstein, M.P. O'Horo, B.N. Ganguly, V. Mehrotra, M.W. Russell, D.R. Huffman, *Science* **257**, 219 (1992).

[8] I. Anton, I. de Sabata, L. Vékás, *J. Magn. Magn. Mater.* **85**, 219 (1990).

[9] K. Raj, B. Moskowitz, R.J. Casciari, *J. Magn. Magn. Mater.* **149**, 174 (1995).

[10] N. Guskos, J. Typek, T. Bodziony, G. Zolnierkiewicz, M. Maryniak, A. Biedunkiewicz, *J. Alloys Comp.* **470**, 51 (2009).

[11] N. Guskos, T. Bodziony, M. Maryniak, J. Typek, A. Biedunkiewicz, *J. Alloys Comp.* **455**, 52 (2008).

[12] N. Guskos, T. Bodziony, A. Biedunkiewicz, K. Aidinis, *Acta Phys. Pol. A* **108**, 311 (2005).

[13] T. Bodziony, N. Guskos, A. Biedunkiewicz, J. Typek, R. Wróbel, M. Maryniak, *Mater. Sci.-Poland* **23**, 899 (2005).

[14] A. Biedunkiewicz, P. Figiel, U. Gabriel, M. Sabara, S. Lenart, *Cent. Eur. J. Phys.* **9**, 417 (2011).

[15] P. Figiel, W. Biedunkiewicz, D. Grzesiak, *J. Therm. Anal. Calorim.* **108**, 979 (2012).

[16] J. Typek, K. Wardal, G. Zolnierkiewicz, N. Guskos, D. Sibera, U. Narkiewicz, *J. Magn. Magn. Mater.* **361**, 12 (2014).

[17] T. Bitoh, K. Ohba, M. Takamatsu, T. Shirane, S. Chikazawa, *J. Phys. Soc. Jpn.* **64**, 1305 (1995).